Reflectometric Measurements of Fibre-based Four-wave mixing Systems

Hao Liu, Kyle R. H. Bottrill, Ali Masoudi, Valerio Vitali, and Periklis Petropoulos

Abstract—A convenient way of achieving polarization-insensitive four-wave mixing in optical fibers is through the use of two orthogonally polarized pumps. However, the interplay between fiber birefringence and the four-wave mixing processes makes polarization insensitivity challenging to achieve. The strict control of the input pumps' states of polarization has been used to minimize polarization sensitivity. Nonetheless, a comprehensive analysis of the complex interplay between birefringence and four-wave mixing, both theoretically and experimentally, is still missing. Here, we adopt an optical time domain reflectometry technique to address this issue by measuring the Rayleigh back-scattered power of the phase-conjugated idler generated by a four-wave mixing process. A system with approximately 50 cm spatial resolution capable of measuring the onset of polarization dependency of orthogonal-pump four-wave mixing systems in the saturation regime is experimentally demonstrated. The obtained results are compared with a detailed fibre model, and close agreement is confirmed. This study will further the understanding of the polarization sensitivity of multi-wave mixing dynamics in optical fibers and support the design of optimized fiber-based parametric devices.

Index Terms—Birefringent fibre, four-wave mixing, optical time-domain reflectometry, Rayleigh scattering

I. INTRODUCTION

FOUR wave mixing (FWM) processes, arising from Kerr nonlinearity in optical fibers, have enabled the demonstration of a large number of all-optical signal processing operations, such as wavelength conversion [1], phase-sensitive amplification [2], and amplitude and/or phase regeneration [3] [4]. There are two main approaches to achieve polarization insensitive operation, namely polarization diversity [5] in degenerate FWM and orthogonal pumping [6] in non-degenerate FWM configurations. The polarization-diversity approach can be implemented simply by a nonlinear loop mirror, but it may be more susceptible to suffering from backscattering power due to counter-propagation. An alternative technique, orthogonal pumping, utilizes two pumps with an orthogonal state of polarization (SoP). This method is uni-directional, making it less susceptible to performance degradation from backscattering, such as Rayleigh scattering, stimulated Brillouin scattering (SBS), and facet reflection from optical components. In both of these approaches, residual birefringence

in the nonlinear medium can lead to a polarization-dependent gain (PDG), degrading system performance. Although, in principle, this effect can be mitigated in polarization diversity schemes through the use of polarization maintaining highly nonlinear fibre (HNLF), this option is not available in the orthogonal pump technique, wherein phase matching must be achieved on orthogonal polarizations at the same time. As such, studying the complex interplay between FWM and birefringence is essential if we are to perfect our control and understanding of such systems. By its nature, birefringence in lowly birefringent fibres varies along the length of the fibre as a stochastic process that is challenging both to measure and model with accuracy. Ideally, a distance-resolved measurement of the FWM process would help to understand the impact of birefringence and determine the accuracy of the modelling. The use of optical time-domain reflectometry (OTDR) systems based on Rayleigh scattering represents one solution to this problem, thanks to the possibility of measuring the spatial evolution of signals without disturbing the actual nonlinear processes.

An early use of OTDR to perform distributed FWM measurements in optical fibres was performed by Ravet et al. [7] [8] who studied the impact of dispersion in degenerate FWM in a dispersion-shifted fibre. More recently, OTDR was utilized to study the broken symmetry of Fermi–Pasta–Ulam Recurrence, where the amplitude and phase of frequency modes were reconstructed via post-processing of the backscattered light in single mode fibre systems [9] [10]. Moreover, a distributed measurement of forward Brillouin scattering involving FWM processes was carried out in an eight km-long length of single mode fibre for Brillouin-based fibre sensors [11]. In our previous work [12], we carried out a numerical investigation on the birefringence effects in an orthogonal-pump FWM system, emphasizing the small signal regime. In particular, we analyzed the spatial evolution of PDG under various levels of fiber birefringence. However, longitudinally resolved measurements of polarization-dependent multi-wave mixing, especially the orthogonally pumped FWM scheme and the dependence of its PDG on birefringence in the saturation regime are yet to be studied.

In this work, we used an OTDR system to measure the Rayleigh backscattered light of the phase-conjugated idler generated by a forward FWM process in the saturation regime, we reported part of the results first in [13], this manuscript significantly extends the scope of the previous work,

providing a detailed and thorough analysis of the methodology, measurements, and numerical results to make it more comprehensive. In Section II, we describe the experimental configuration and the modeling methodologies we used in this study. We validated the system by measuring the evolution of Rayleigh backscattered idler power in both a single-pump and a co-polarized dual-pump scheme and comparing it to the numerical results of the modeling. In Section III, we analyze the experimental results with the aid of the modeling and identify three special cases where the input SoP of the signal leads to an interesting evolution of the idler power. We then investigate the PDG in the orthogonal-pump FWM scheme, in particular, how the onset of saturation of the FWM gain affects PDG. Our results show that the onset of saturation depends on the signal SoP and that saturation itself leads to a strong increase in PDG. In Section IV, we further numerically investigate the underlying interplay between birefringence and FWM by also looking at the pump power and relative SoP evolution between the two pumps in an orthogonal-pump FWM system. The presented results indicate that, in the saturation regime, the degree of co-polarization (DoC) between the two pumps is affected by the input signal's SoP. Furthermore, the additional increase of the PDG is closely associated with the polarization-dependent variation of the DoC traces that occur as the input signal's SoP varies.

II. METHODOLOGY

A. Experimental setup

The experimental setup used for the distributed measurement of the phase conjugated idler generated in the orthogonal-pump FWM process is shown in Fig. 1. The pulsed signal generation stage was designed to have high polarization stability and high amplified spontaneous emission (ASE) noise rejection, whilst the detection system was designed to maximise the sensitivity to the weak Rayleigh-backscattered light. Two continuous-wave (CW) laser sources, denoted as P_1 and P_2 in Fig. 1 (at wavelengths 1546.2 nm and 1552.6 nm), were used as the two pumps of the nonlinear process. The selection of these two pump wavelengths is mainly based on the availability of (dense wavelength division multiplexing) DWDM filters in our laboratory. Additionally, the center wavelength of the fiber Bragg grating (FBG) requires the phase-conjugated idler to be centered around 1550 nm, which limits the choice of the signal wavelength. To increase flexibility, alternative center wavelengths of DWDM filters and FBGs should be adopted. Furthermore, it's worth noting that tunable bandpass filters can also serve as an effective solution for suppressing ASE noise. In our experiment, DWDM serves as a straightforward ASE noise filtering method, while FBG, readily available in our laboratory, offers exceptionally narrow linewidth filtering. To delay the onset of stimulated Brillouin scattering (SBS) and reduce coherent Rayleigh noise (i.e. interference in the backscattered light originating from different parts of pulse) [13] [14] in the HNLF, the linewidths of the two pump sources were broadened through phase modulation. Two phase modulators (PMs) were utilized to independently modulate the phase of two pumps, driven by an 8 GSa/s,
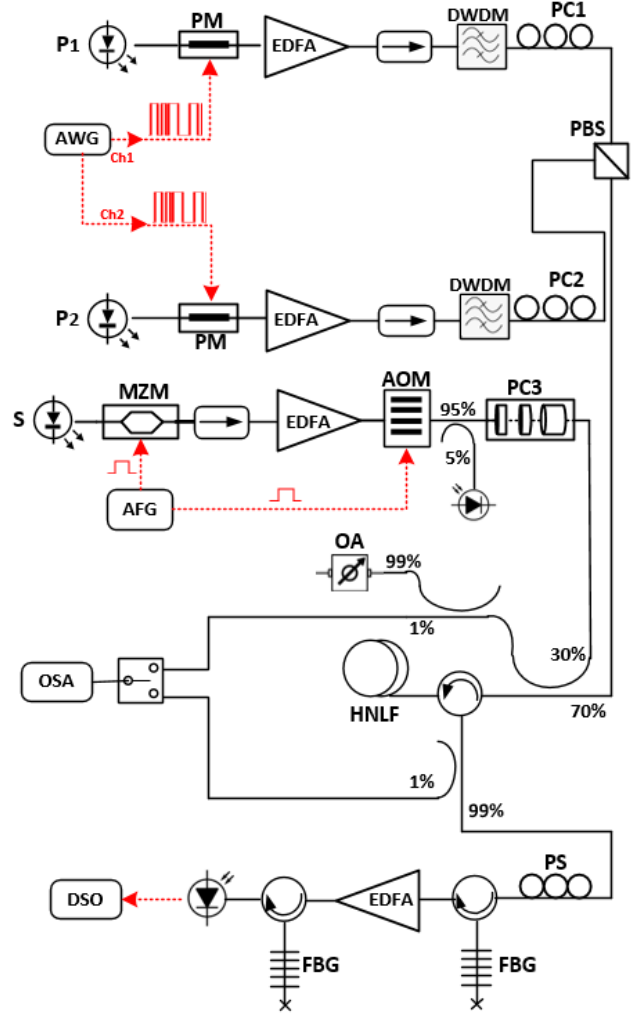

Fig. 1. OTDR-based orthogonal-pump FWM system setup; PM: phase modulator; EDFA: Erbium-doped fibre amplifier; DWDM filter: Dense wavelength division multiplexing filter; PBS: polarization beam splitter; PC(1,2,3): polarization controller (1,2,3); MZM: Mach-Zehnder modulator; AFG: Arbitrary function generator; AOM: Acousto-optic modulator; OA: optical attenuator; OSA: optical spectrum analyzer; PS: polarization scrambler; FBG: Fibre Bragg grating; DSO: digital storage oscilloscope; HNLF: Highly nonlinear fibre

$2^{15}-1$, pseudo-random binary bit sequence (PRBS), generated from an arbitrary waveform generator (AWG). Through the characterization of the input pump and backscattered power spectrum, it was observed that the Brillouin threshold value for P_1 is at least 31 dBm, whereas for P_2, it is around 27 dBm. Consequently, for the HNLF-based dual-pump system, the power associated with each pump before the HNLF was set below these values. Polarization controllers (PCs) and a polarization beam splitter (PBS) were used to ensure the two pump SoPs were orthogonal when launched into the HNLF (from Furukawa Electric Ltd., specifications as shown in Tab. I).

The signal in the FWM process was generated by a narrow linewidth laser (λ = 1548.8 nm), carved into a pulse train of 5 ns wide pulses with a period of 15 μs. This pulse duration enabled us to obtain OTDR traces with approximately 50 cm spatial resolution for the measured 500 m long HNLF.

$$\frac{\partial E_x}{\partial z} + \frac{\alpha}{2}E_x - i\frac{\beta_{xy}}{2}E_x + \frac{\beta_{xy}'}{2}\frac{\partial E_x}{\partial t} - \sum_{n=2}^{3}\frac{i^{n+1}\beta_x^{(n)}}{n!}\frac{\partial^n E_x}{\partial t^n} = i\gamma(|E_x|^2 E_x + \frac{2}{3}|E_y|^2 E_x + \frac{1}{3}(E_y)^2 E_x^*)$$

$$\frac{\partial E_y}{\partial z} + \frac{\alpha}{2}E_y + i\frac{\beta_{xy}}{2}E_y - \frac{\beta_{xy}'}{2}\frac{\partial E_y}{\partial t} - \sum_{n=2}^{3}\frac{i^{n+1}\beta_y^{(n)}}{n!}\frac{\partial^n E_y}{\partial t^n} = i\gamma(|E_y|^2 E_y + \frac{2}{3}|E_x|^2 E_y + \frac{1}{3}(E_x)^2 E_y^*)$$

(1)

TABLE I
HNLF SPECIFICATIONS

Parameters	Values	Units
Length L	500	m
Effective nonlinear coefficient γ	11	$W^{-1}\cdot m^{-1}$
2nd order dispersion β_2	0.06	$ps/nm/km$
3rd order dispersion β_3	0.0035	$ps/nm^2/km$
Attenuation α	1.44	dB/km
Polarization-mode dispersion (PMD)	0.139	$ps/\sqrt{km}$

GSa/s Digital Storage Oscilloscope (DSO). A programmable polarisation controller (PC3) enabled measurements to be taken on each one of 64 different SoPs (spread uniformly around the Poincaré sphere) for the input signal. The signal was coupled together with the pumps in the HNLF by means of a 70:30 coupler. The OSA was primarily utilized for basic monitoring of the pump wavelength positions and the phase modulation of the two pumps, as well as for monitoring and assisting in optimizing the input pump power levels. The Rayleigh backscattered light from the HNLF was then sent to a 70 kHz polarization scrambler (PS) (to remove any polarization-dependent effects from the EDFA that followed) and through a FBG filter (λ = 1550.1 nm, 5 GHz bandwidth and 99% reflectivity) to reject the Rayleigh back-scattered light resulting from the propagation of the pumps and signal. The filtered idler was then amplified using an EDFA (to improve the receiver sensitivity) before undergoing a final stage of filtering (to suppress ASE noise from the EDFA), after which it was detected by a photodiode with a 40 kΩ trans-impedance amplifier and recorded by the DSO for offline post-processing.

B. Numerical modeling

The experimental set-up described above was used to study the longitudinal evolution of the idler wave along the length of the HNLF. To better interpret the experimental results, numerical modeling of the FWM system was carried out. Here, we describe the way we performed the modeling. The Coupled Nonlinear Schrödinger equation (C-NLSE) [15] is a powerful and flexible tool that has been widely used to study pulse propagation in optical fibres. In a randomly and linearly varying birefringent HNLF, the evolution of the slowly varying electric field envelopes E_x and E_y propagating in two orthogonal polarizations is governed by the C-NLSE in the time domain (shown in equation (1)), where α represents the linear loss, γ represents the nonlinear coefficient, $\beta_{xy}/2$

denotes the half of the difference between the propagation constants along the x- (β_x) and y-axis (β_y), which is related to the modes' phase velocities, and $\beta_{xy}'/2$ represents the frequency-dependent birefringence, which is related to the modes' group velocities. Group velocity dispersion $\beta_x^{(2)}$, $\beta_y^{(2)}$ and third order dispersion $\beta_x^{(3)}$, $\beta_y^{(3)}$ are described using the fifth term on the left-hand side of equation (1), while the three nonlinear birefringence terms on the right-hand side describe the self-phase modulation (SPM) [16], cross-phase modulation (XPM) [16] and ellipse rotation [16]. All of the terms shown in equation (1) were included in the modelling, whereas Brillouin scattering effects were neglected, since they were suppressed in the experimental measurements by using the pump phase dithering technique, and Raman scattering was also ignored, since pump-to-pump and signal-to-pump spacings were small in our experiments.

To simulate a 500 m long weakly birefringent fiber with continuous variation in birefringence, we divided the fiber into 1000 short segments. This was found to be sufficient to accurately capture small variations in birefringence along the entire length and achieved good convergence of the results. β_{xy} and β_{xy}' differed in each fibre segment and were assigned in accordance with the used birefringence model. The rotation angle of the birefringent axis was introduced at the beginning of each fibre segment. β_{xy}, β_{xy}' and birefringent axis rotation angle were modelled using the Random modulus model (RMM) [17], since this model has been shown to offer good agreement with experimental results [18]. This model assumes that the first two components of the birefringence vector independently obey the Langevin equation [17] and allows fibres to be modelled with a birefringence that varies randomly along the fibre length, determined by two parameters: the beat length L_b and correlation length L_c. L_b represents the length scale over which a signal returns to its original SoP. L_c represents how fast the random birefringence perturbation changes [17]. The two pump SoPs were launched in horizontal (along the x axis) and vertical (along the y axis) polarizations in the HNLF, while PDG was defined and calculated by finding the difference between maximum and minimum idler power as the signal SoP was varied [12]. 64 different signal SoPs scattered on the Poincaré sphere were used to obtain the converged PDG value [12]. For the particular fibre used in the experiments, it was found that there is close agreement between simulation and measurement results when using L_c = 100 m, while assuming L_b = 10 m [19]. This is a reasonable assumption considering the PMD value of this fibre (Tab. I). The maximum idler power value was found by varying the input signal SoP. The simulated idler power traces were normalized to the maximum idler power value to simplify the
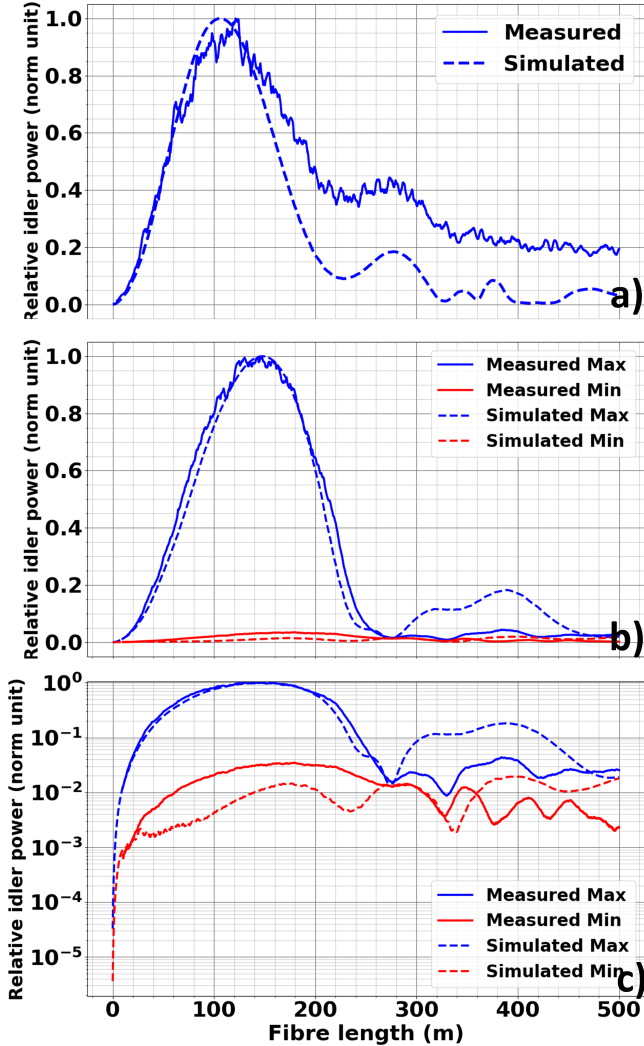
Fig. 2. (a) Degenerate FWM system; Measured (solid trace in blue) and simulated (dashed trace in blue); pump power: 1445.4mW; peak signal power: 583.4mW; pump wavelength: 1552.8nm; signal wavelength: 1555.7nm.(b) Dual co-polarized pump FWM system; measured maximum (solid trace in blue) and minimum (solid trace in red); simulated maximum (dashed line in blue) and minimum (dashed line in red); total pump power: 952.2 mW; peak signal power: 70.8 mW; two pump wavelengths: 1546.2nm and 1552.6nm; signal wavelength: 1548.8nm.(c) Figure 2(b) with a logarithmic y-axis

comparison between the experimental and numerical results which will be discussed in the following section.

C. Comparison between modelling and experimental results

In order to test the validity of our modeling results, we carried out a comparison study with the measurements obtained from the experiments. Since the Rayleigh backscattered idler power was measured in our set-up (see Section II.A), we needed to calculate the forward transmission power from the backscattered measurements. To achieve this, the fibre loss (1.44 dB/km) was used in an estimation procedure. Then all the measured idler power traces were also normalized to their maximum power value. A numerical simulation based on the fibre parameters shown in Tab. I was carried out to obtain a comparison with the experimental measurements. To

confirm the correct operation of the measuring system and the system's ability to measure sufficiently large PDGs, we initially studied the degenerate FWM system configuration, where two co-polarized sources for the signal (1555.7 nm) and the pump (1552.8 nm) were used. Fig. 2 (a) compares the experimentally measured and numerically simulated idler power traces. The traces show good agreement up to the first saturation point. The discrepancy observed beyond this point may be attributed to the longitudinally varying dispersion in the HNLF, which was not considered in the numerical simulations. The comparison shows the significant influence of both dispersion and birefringence once the onset of saturation has been reached.

Next, a dual co-polarized pump configuration was considered, which required only minor modifications to be made to the system setup of Fig. 1. By varying the signal SoP, we measured both the case where the signal was co-polarized with the pumps (maximum conversion efficiency) and the case where it was orthogonal to the pumps (minimum conversion efficiency). As expected (Fig. 2(b)), this latter arrangement resulted in a strong suppression of the idler power, with a PDG of 13 dB measured between the peaks of the curves. As before, close agreement between experimental measurements and numerical simulations was found up to the saturation point.

III. RESULTS

We used the set-up shown in Fig. 1 to perform a distributed characterization of the orthogonally-pumped FWM system. Four different pump power levels (total pump power of 374 mW, 574 mW, 726 mW and 1105 mW) were used to study the polarization dependency of the idler as the signal SoP was varied, where each pump possesses half of the total pump power. The resulting spatial evolution curves of the idler show that both the saturated idler power and the distance along the fibre at which the saturation is reached vary with the signal SoP. In particular, we can identify the curves with 1) a signal SoP leading to the maximum saturated idler power, 2) a signal SoP leading to the minimum saturated idler power and 3) a signal SoP leading to the earliest onset of saturation along the fibre length for different pump power levels. This procedure was carried out for both the experimental measurements and the numerical simulations. It needs to be noted that the dashed traces with the same color in Fig. 3(a-d) have the same input signal SoP.

In addition, the simulation results indicate that saturation occurs sooner when the signal has a SoP that is 45° relative to the two orthogonal pumps. Therefore, we identify the curve that saturates the soonest in the experiments as possessing this 45° relative polarization. Amongst the results, we observed idler power traces with varying shapes, breadth, and flatness. This rich variation highlights the potential for exploiting different SoP inputs to achieve more robust squeezing performance and enable flexible design in saturation-based amplitude limiters.

In Fig. 3(e), a plot of the PDG evolution as a function of the fibre length is shown, which was obtained by calculating
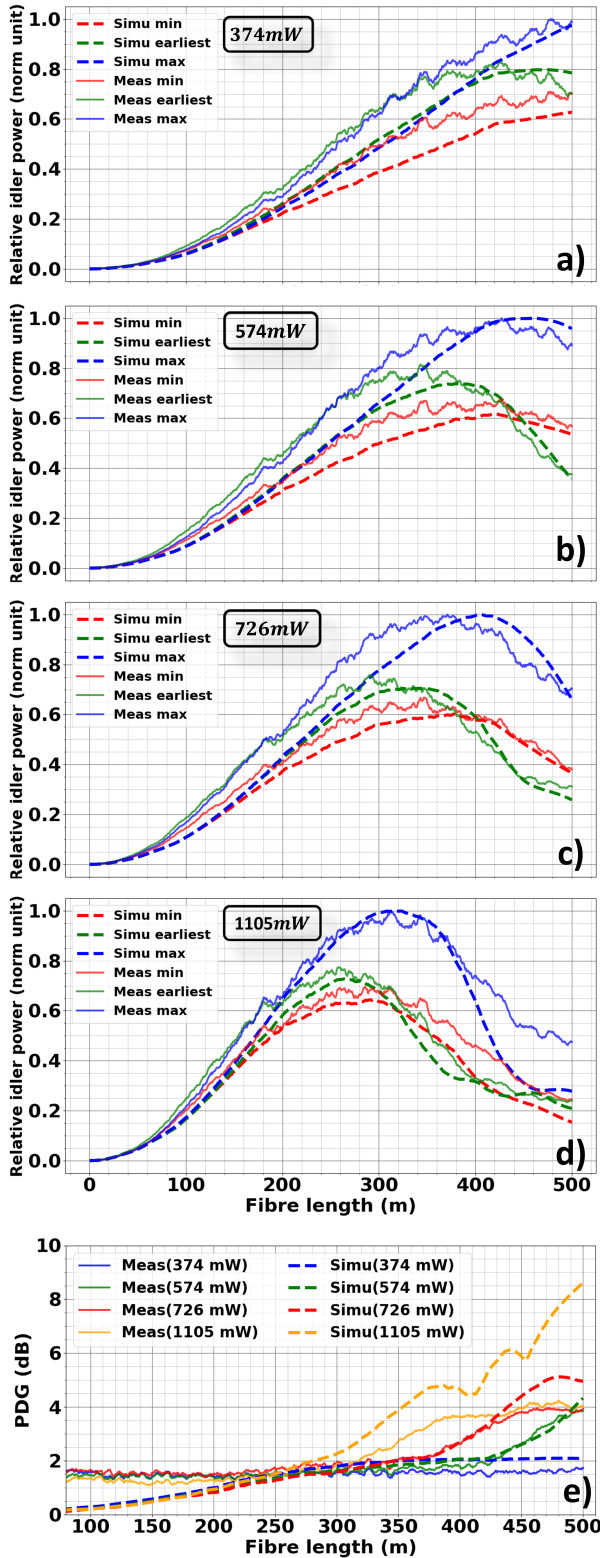
Fig. 3. Measured and simulated minimum (solid trace and dashed lines in red), maximum (solid trace and dashed lines in blue) and earliest (solid trace and dashed lines in green) idler saturation curves using (a) 374 mW, (b) 574 mW, (c) 726 mW total pump power and (d) 1105 mW total pump power; the input signal peak power is fixed at 108mW; (e) measured (solid trace) and simulated (dashed line) PDG evolution curves for the four different total pump power levels shown in the legend.

the difference between the measured maximum and minimum idler power values from the 64 signal SoPs. These data show that saturation of the FWM process is associated with an increase in PDG and should therefore be avoided for most applications. As expected, as pump powers increase, the onset of saturation is met earlier in the fibre. Hence, PDG begins to grow sooner. The numerical simulations predicted the same onset distance as the experimental results, further supporting the modelling.

The discrepancy between numerical and experimental results before 200 m can be attributed to the low signal-to-noise ratio (SNR) of the Rayleigh backscattered idler at the beginning of the fibre, which limits the lowest measurable PDG value, as well as the fraction of polarized ASE noise that is not suppressed by the DWDM filter.

IV. DISCUSSION

After confirming the model's good predictive ability by comparing it with the experimental results, we can gain insight into the cause of PDG by including the pump power and SoP evolution in the modelling. In the numerical simulations presented in this section, we assumed that the fibre was dispersionless, allowing us to isolate the discussion of the polarization sensitivity that the phase-conjugated idler suffers from dispersion. The rest of the fibre parameters were derived from Tab. I and all of the system parameters were kept the same as in the experimental implementation described in Section II.A. Comparing the simulated idler power traces in Fig 4 (a) and the PDG trace in Fig 4 (b) with the experimentally measured idler power traces in Figure 3 (a) and PDG trace in Fig. 3 (d), we observe a similar trend. This indicates that the role of dispersion in the process is weak and that the assumptions made are valid.

We obtained power traces for the pump and idler at two different total pump power levels (374 mW and 1105 mW) and present them in Fig. 4 (a) and (c), respectively. Both pump and idler power traces were normalized to the maximum pump power. To simplify the presentation, only the maximum (dotted blue), minimum (dotted red), and earliest saturated (dotted green) idler traces are shown, as was the case in the presentation of the experimental measurements in Section III. The corresponding pump power traces are plotted using solid traces. As the pump spacing is small, only one of the pump power traces (that of the short-wavelength pump) is shown. Furthermore, we used the DoC and PDG to analyze the polarization sensitivity of the idler propagating along the optical fibre. DoC is defined as the dot product of two pumps' SoP ($\vec{S_1} \cdot \vec{S_2}$) [20]. By varying the input signal SoPs, we were able to obtain three different DoC traces (dotted blue, red, and green traces) that correspond to the maximum, minimum, and earliest saturated idler power traces, as shown in Fig. 4 (b) and (d).

Fig 4 (a) and Fig 4 (c) show a correlation between the rate of increase of idler power and the depletion rate of the pump power. Both pump and idler power traces exhibit polarization-dependent variations. By comparing Figure 4 (a) with Figure 4 (b), we can observe a similar trend between the three idler
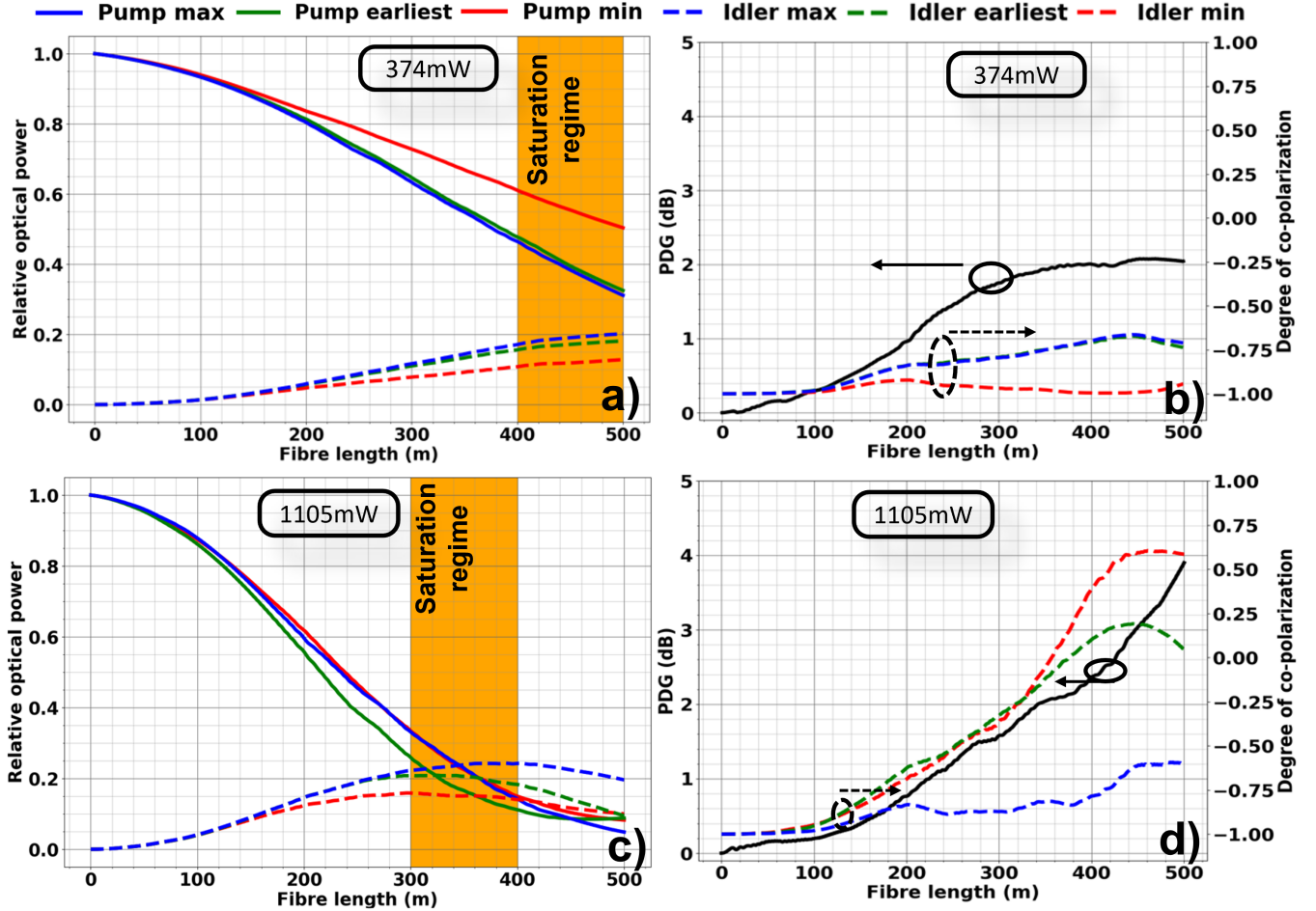
Fig. 4. Simulated idler power traces with the maximum (dotted blue), minimum (dotted red), and earliest saturation (dotted green) curves, using two different total pump power levels: (a) 374 mW and (c) 1105 mW. Solid blue, red and green traces show the corresponding pump power traces for the maximum, minimum and earliest saturation idler traces. Also shown are the simulated PDG evolution trace (solid black) and three DoC traces corresponding to the maximum (dotted blue), minimum (dotted red) and earliest saturation (dotted green) idler traces, using the same two pump power levels: (b) 374 mW and (d) 1105 mW. The peak power of the pulsed signal at the fibre input was fixed at 108 mW for all the considered cases.

power traces and DoC traces. Interestingly, we can observe a significant increase in the PDG, the evolution of which depends on the relative difference between the maximum and minimum DoC traces between the two pumps. In contrast, for the orthogonal-pump FWM system in the small signal regime we studied [12], DoC will not exhibit polarization-dependent variation when the input signal power is much lower than the input pump power. Therefore, we can understand that when we use large signal power at the fibre input, the relative SoPs of the two pumps will be affected by the input signal SoP. Depending on the relative SoP between the input signal and the two pumps, the relative SoP evolution of the two pumps will also become polarization-dependent. Thus, we will get the additional PDG increase in the saturation regime coming from the polarization-dependent variation of the DoC between the two pumps. This characteristic can be evidenced further in Fig. 4 (d). We observe a close relationship between the increase in PDG and the relative difference between the maximum and minimum DoC traces until the point where the pump

power levels become lower than the idler power levels. After this point, we attribute the further increase in PDG to the unpredictable and unstable reversal of the power flow in the orthogonal-pump FWM process.

V. CONCLUSIONS AND OUTLOOK

We demonstrated an OTDR-based characterization of both degenerate and non-degenerate FWM systems, capable of measuring the polarization dependency of a Rayleigh-backscattered idler. The saturation regime in an orthogonally-pumped FWM system for the idler power was investigated considering different pump power levels and input signal SoPs. A good match between numerical simulations and experimental results was found when comparing the extreme cases of maximum, minimum and earliest saturation curves. Characterizing the behaviour of fibres with this measurement system can assist the optimization of a range of FWM-based signal processing schemes, including wavelength converters, optical phase conjugators and particularly, it benefits schemes

relying on the onset of FWM saturation, such as saturation-based amplitude limiters. Moreover, the presented theoretical analysis explains the rapid increase of PDG in the saturation regime. Finally, we also believe that the confirmation of the numerical model reliability and the performance of the measurement scheme will allow further in-depth studies into the complex effects that birefringence has on FWM systems.

ACKNOWLEDGMENTS

REFERENCES

[1] S. Watanabe, T. Kato, T. Tanimura, C. Schmidt-Langhorst, R. Elschner, I. Sackey, C. Schubert, and T. Hoshida, "Wavelength conversion using fiber cross-phase modulation driven by two pump waves," *Optics express*, vol. 27, no. 12, pp. 16 767–16 780, 2019.

[2] P. A. Andrekson and M. Karlsson, "Fiber-based phase-sensitive optical amplifiers and their applications," *Advances in Optics and Photonics*, vol. 12, no. 2, pp. 367–428, 2020.

[3] F. Parmigiani, G. Hesketh, R. Slavík, P. Horak, P. Petropoulos, and D. J. Richardson, "Polarization-assisted phase-sensitive processor," *Journal of Lightwave Technology*, vol. 33, no. 6, pp. 1166–1174, 2015.

[4] K. R. Bottrill, N. Taengnoi, Y. Hong, D. Richardson, and P. Petropoulos, "Phase preserving amplitude saturation through tone synthesis assisted saturated four-wave mixing," *Journal of Lightwave Technology*, vol. 38, no. 7, pp. 1817–1826, 2020.

[5] M. Stephens, V. Gordienko, and N. Doran, "20 dB net-gain polarization-insensitive fiber optical parametric amplifier with > 2 THz bandwidth," *Optics Express*, vol. 25, no. 9, pp. 10 597–10 609, 2017.

[6] V. J. Rancaño, F. Parmigiani, P. Petropoulos, and D. J. Richardson, "100 GHz grid-aligned reconfigurable polarization insensitive black-box wavelength converter," in *Optical Fiber Communication Conference*. Optica Publishing Group, 2013, pp. JTh2A–19.

[7] G. Ravet, F. Vanholsbeek, P. Emplit, M. Wuilpart, and P. Mégret, "OTDR technique for the characterization of FWM processes in optical fibers," in *IEEE Laser and Electro-Optics Society Symposium*, 2007, pp. 203–206.

[8] G. Ravet, A. Mussot, M. Wuilpart, A. Kudlinski, C. Caucheteur, and P. Mégret, "Distributed measurement of modulation instability along optical fibers," in *IEEE Photonics Society Summer Topicals 2010*. IEEE, 2010, pp. 166–167.

[9] A. Mussot, C. Naveau, M. Conforti, A. Kudlinski, F. Copie, P. Szrift-giser, and S. Trillo, "Fibre multi-wave mixing combs reveal the broken symmetry of Fermi–Pasta–Ulam Recurrence," *Nature photonics*, vol. 12, no. 5, pp. 303–308, 2018.

[10] X. Hu, W. Chen, Y. Lu, Z. Yu, M. Chen, and Z. Meng, "Distributed measurement of Fermi–Pasta–Ulam Recurrence in optical fibers," *IEEE Photonics Technology Letters*, vol. 30, no. 1, pp. 47–50, 2017.

[11] Y. London, H. H. Diamandi, G. Bashan, and A. Zadok, "Invited article: distributed analysis of nonlinear wave mixing in fiber due to forward Brillouin Scattering and Kerr effects," *APL Photonics*, vol. 3, no. 11, p. 110804, 2018.

[12] H. Liu, K. R. Bottrill, V. Vitali, A. Taranta, and P. Petropoulos, "Quantitative study of birefringence effects in fiber-based orthogonal-pump FWM systems," *Optics Express*, vol. 31, no. 4, pp. 5801–5811, 2023.

[13] A. Masoudi and T. P. Newson, "Analysis of distributed optical fibre acoustic sensors through numerical modelling," *Optics express*, vol. 25, no. 25, pp. 32 021–32 040, 2017.

[14] L. D. van Putten, A. Masoudi, J. Snook, and G. Brambilla, "Numerical modelling of a distributed acoustic sensor based on ultra-low loss-enhanced backscattering fibers," *Sensors*, vol. 21, no. 20, p. 6869, 2021.

[15] M. Marhic, A. Rieznik, G. Kalogerakis, C. Braimiotis, H. Fragnito, and L. Kazovsky, "Accurate numerical simulation of short fiber optical parametric amplifiers," *Optics express*, vol. 16, no. 6, pp. 3610–3622, 2008.

[16] M. E. Marhic, *Fiber optical parametric amplifiers, oscillators and related devices*. Cambridge university press, 2008.

[17] P. K. A. Wai and C. Menyak, "Polarization mode dispersion, decorrelation, and diffusion in optical fibers with randomly varying birefringence," *Journal of Lightwave Technology*, vol. 14, no. 2, pp. 148–157, 1996.

[18] A. Galtarossa, L. Palmieri, M. Schiano, and T. Tambosso, "Statistical characterization of fiber random birefringence," *Optics Letters*, vol. 25, no. 18, pp. 1322–1324, 2000.

[19] C. R. Menyuk and B. S. Marks, "Interaction of polarization mode dispersion and nonlinearity in optical fiber transmission systems," *Journal of Lightwave Technology*, vol. 24, no. 7, p. 2806, 2006.

[20] Q. Lin and G. P. Agrawal, "Vector theory of four-wave mixing: polarization effects in fiber-optic parametric amplifiers," *JOSA B*, vol. 21, no. 6, pp. 1216–1224, 2004.